Contents lists available at ScienceDirect

Chemical Engineering Journal

journal homepage: www.elsevier.com/locate/cej



An UV to NIR-driven platform based on red phosphorus/graphene oxide film for rapid microbial inactivation



Qi Zhang^a, Xiangmei Liu^{a,*}, Lei Tan^a, Zhenduo Cui^b, Zhaoyang Li^b, Yanqin Liang^b, Shengli Zhu^b, K.W.K. Yeung^c, Yufeng Zheng^d, Shuilin Wu^b

- a Ministry-of-Education Key Laboratory for the Green Preparation and Application of Functional Materials, Hubei Key Laboratory of Polymer Materials, School of Materials Science & Engineering, Hubei University, Wuhan 430062, China
- ^b School of Materials Science & Engineering, Tianjin University, Tianjin 300072, China
- ^c Department of Orthopaedics & Traumatology, Li KaShing Faculty of Medicine, The University of Hong Kong, Pokfulam, Hong Kong 999077, China
- d State Key Laboratory for Turbulence and Complex System and Department of Materials Science and Engineering, College of Engineering, Peking University, Beijing 100871, China

HIGHLIGHTS

- A RP/GO composite array of irregular pyramids was successfully synthesized on Ti.
- The GO layer obviously enhanced the photoelectrochemical performance of RP film.
- The RP/GO hybrid exhibited a broad absorption along with a broad spectral response.
- Photodynamic and photothermal effects synergistically lead to excellent disinfection.
- Simple synthesis, stable disinfection and non-toxicity cause practical importance.

ARTICLE INFO

Keywords: Disinfection Photocatalytic Photothermal Red phosphorus Broad spectral response

ABSTRACT

The problem of bacterial infection is getting worse. Photo-driven disinfection is an effective solution with the perspective of energy consumption. However, the current researches focus on expanding the utilization of light energy from ultraviolet to visible light, while the infrared portion of sunlight has not been considered. Thus, it is desirable to develop novel materials, with a broader solar spectrum utilization, for rapid microbial inactivation. Here we show a crystalline phosphorus film consist of irregular pyramids covered by graphene oxide with an enhanced photoelectrochemical performance. The metal-free film exhibits broad absorption throughout the solar spectrum with good photocatalytic and photothermal properties. With the synergy of photodynamic and photothermal effects, the composite exhibited inactivation of about 99.9% on Staphylococcus aureus and Escherichia coli within 20 min of simulated sunlight irradiation. Meanwhile, well disinfection were also exhibited under visible and 808 nm light. By the way, good biocompatibility, along with excellent biofilm removal under LED light, provided the film a prospect in disinfection of medical devices.

1. Introduction

Bacterial infections lead to death worldwide [1,2], in which waterborne diseases are among the prominent [3,4]. In recent years, the situation has worsened, due to the resistance come from the extensive use of traditional antibacterial agents [2,3]. For the traditional methods of drinking water disinfection, ultraviolet irradiation and chlorine microbial degradation have been widely used [3,5]. However, several serious drawback are there, such as photo-corrosion problems, low light

utilization, and carcinogenic by-products [5]. Hence, a microbial inactivation method, with efficiently energy-utilization and environmentally friendliness, is urgently needed.

The way of photocatalytic disinfection based on semiconductors attracts increased interest, due to the perspective of energy consumption and low toxicity [3,6]. Reactive oxygen species (ROS) generated from photocatalysts can inactivate pathogens by destroying essential macromolecules [7,8], even on drug-resistant strains [9,10]. However, the photocatalysts studied are mostly metal compounds, such as TiO2

E-mail address: liuxiangmei1978@163.com (X. Liu).

^{*} Corresponding author.

[6], ZnO [7], and MoS₂ [11,12]. And the utilization of sunlight are limited to ultraviolet or visible light, with long inactivation time or low microbial concentration. The infrared light (account for 52% of the energy of sunlight) is ignored. Besides, the metal elements may bring potential biosafety risks [8]. Additionally, photothermal sterilization, in which microbes would be effectively inactivated at a higher temperature, is also a promising and effective alternative, especially combined with the photocatalysis [13]. Meanwhile, it is an important way to improve the utilization of sunlight in near-infrared portion [14].

Recently, the semiconductors based on phosphorus (P) have attracted more and more attention because of the wide distribution in earth and environmentally friendly property [15]. Up to now, various P allotropes have been recognized to possess photocatalytic activities. such as black P [16,17], amorphous red P (RP) [18,19], Hittorf's RP [20], and fibrous RP [21,22]. Among them, because of cheap raw materials amorphous RP is more widely studied as photocatalysis in H2 evolution [23,24], fuels production [25], bacterial inactivation [26,27], and pollutants photodegradation [28,29]. Meanwhile, many efforts have been done for improving the photocatalytic ability, such as loading co-catalyst [30], constructing heterojunctions [31,32,33], improving surface roughness [34], forming imperfections and disordering on surface [27], enhancing surface area [19,35]. In addition, fibrous RP has been reported to own the highest H2 evolution record in the family of elemental photocatalyst [36]. Indications are there that RP is a hot and promising photocatalyst because of low cost, easy availability and low toxicity. Furthermore, complex and numerous molecular structures of P allotropes would means many different or unknown properties [15]. Based on the advantages, it has been used for implantable medical devices in our previous study [13].

In this work, we constructed a crystalline P film on Ti plate (Ti-RP) by chemical vapor deposition (CVD), using the low-cost commercial RP as precursor. The film exhibited a broad absorption throughout the solar spectrum, with good photocatalytic and photothermal properties. Furtherly, graphene oxide (GO) layer was deposited on the RP film to form a hybrid (Ti-RP/GO) to enhance the photoelectrochemical (PEC) properties. And the Ti-RP/GO hybrid showed rapid inactivation about 99.9% and 98.28% to Staphylococcus aureus (S. aureus) of 8×10^6 and 4×10^7 CFU/mL in 20 min under simulated sunlight (SSL), while 99.91% to 1×10^7 CFU/mL Escherichia coli (E. coli) in 15 min. We ulteriorly explored the antibacterial effect under visible and near-infrared light (808 nm), and found well microbial inactivation effect of both. Moreover, inspired by the good biocompatibility and energy conservation, we also employed the LED light to explore the biofilm removal ability of Ti-RP/GO for the application on non-implantable medical devices. Based on the simple synthesis, efficient and stable disinfection, as well as non-toxicity, the film exhibited practical importance for disinfection of water and medical devices.

2. Experimental section

2.1. Synthesis of Ti-RP/GO

A two-step method was employed to prepare Ti-RP/GO. (I) CVD of commercial RP after hydrothermal treatment (RP powder). (II) Heating transition of Shellac [37]. For comparison, the samples of Ti-RP and Ti-GO were also synthesized by the same corresponding process. The details are available in Supplementary data.

2.2. Characterization

The scanning electronic microscopy (SEM) images were carried out by Field-emission SEM (FESEM) (Zeiss sigma 500, Germany) and JSM-6510LV electron microscope (JEOL, Japan). The transmission electron microscope (TEM) images were acquired with Talos F200S equipped with energy-dispersive spectroscopy (EDS) and ZEISS Libra 200 FE transmission electron microscope, all the TEM samples were prepared

by removing the films with a blade. A confocal Raman microspectroscope (Renishaw, UK) was used for Raman spectra. An X-ray diffraction spectrometer (D8A25, Bruker, Germany) was employed for X-ray diffraction patterns (XRD). X-ray photoelectron spectra (XPS) were acquired on an ESCALAB 250Xi instrument (Thermo Scientific, USA). The diffuse reflectance spectra were investigated by a spectrophotometer (UV–Vis-NIR, UV-3600, Shimadu, Japan). A fluorescence spectrophotometer (Perkin Elmer LS55, USA) was employed for photoluminescence spectra (PL). Water contact angles of the samples were carried out under ambient condition with a JC2000D contact angle system (POWEREACH, China). The simulated sunlight (SSL) was obtained from a 300 W Xe lamp (PLS-SXE300, Beijing Changming Technology Co., LT, China), while the 808 nm light was provided by a semiconductor laser source (808 nm, LOS-BLD-0808, 0.25 W/cm²) and the LED light was offered by a LED light source (PLS-LED100B, 0.1 W/cm²).

2.3. Photoelectrochemical measurements

All the photoelectrochemical (PEC) experiments were conducted by a conventional three-electrode. Counter electrode was Pt electrode while reference electrode was Ag/AgCl electrode. The PEC performance of the samples were measured in 0.1 M $\rm Na_2SO_4$ solution with an electrochemical analyzer (CHI-660E, Shanghai Chenhua). SSL was the light source.

2.4. Photothermal effect measurement

The experiments was conducted under the irradiation of SSL $(0.2\,\mathrm{W/cm^2}$ or $0.6\,\mathrm{W/cm^2})$ with the samples put in a 96-well plate. The tests with samples in water and air were both done. The temperature images were obtained by an FLIR thermal imaging camera E50 (FLIR Systems Inc, USA). The points in the curves were obtained from the average temperature by selecting a fixed area on the images in the software FLIR Tools. Meanwhile, the temperature curves under irradiation of 808 nm light or LED light were also obtained when the antibacterial experiments.

3. Results and discussion

3.1. Characterization

Fig. 1A presented the schematic illustration of the two-step route synthetic process for the RP/GO film. Fig. 1B showed the digital photograph of the samples. After CVD treatment, Ti-RP showed a pyramid shaped structure with roughly uniform density and even spatial distribution (Fig. 1C), compared to the smooth Ti surface (Fig. S1A). The insert image in Fig. 1C further revealed irregular pyramid shape of the unit in RP film. After the deposition of GO layer, Ti-RP/GO still retained the general morphology of the original RP film, except a relatively rough surface (Fig. 1D). As comparison, Ti-GO showed a uniform and compact film (Fig. S1B). This could be due to the great film-forming ability of shellac, which made transformed GO able to tightly adhere on the substrates, and then provided well interface contact. Furthermore, the thickness of the pyramids part of the RP/GO film was about 0.65 µm, while that was 0.60 µm for Ti-RP (Fig. S2). Fig. 1E demonstrated that the composited unit of the RP film was tapering. Moreover, RP showed crystalline, with a lattice spacing of 0.175 nm (Fig. 1F). And Fig. S3A and B showed that GO was sheet and amorphous, which was the same as the report of GO from shellac [37]. Furthermore, Fig. 1G showed that the microstructure of RP was not changed. The elements mapping of C and P further demonstrated homogeneously distributed on the surface of the hybrid (Fig. 1H). Fig. 1I showed the lattice spacing of 0.175 nm with some amorphous substances attached on. This proved an interface contact between RP and GO, which provides the possibility for electron transfer. And the similar fast Fourier transforms of RP and

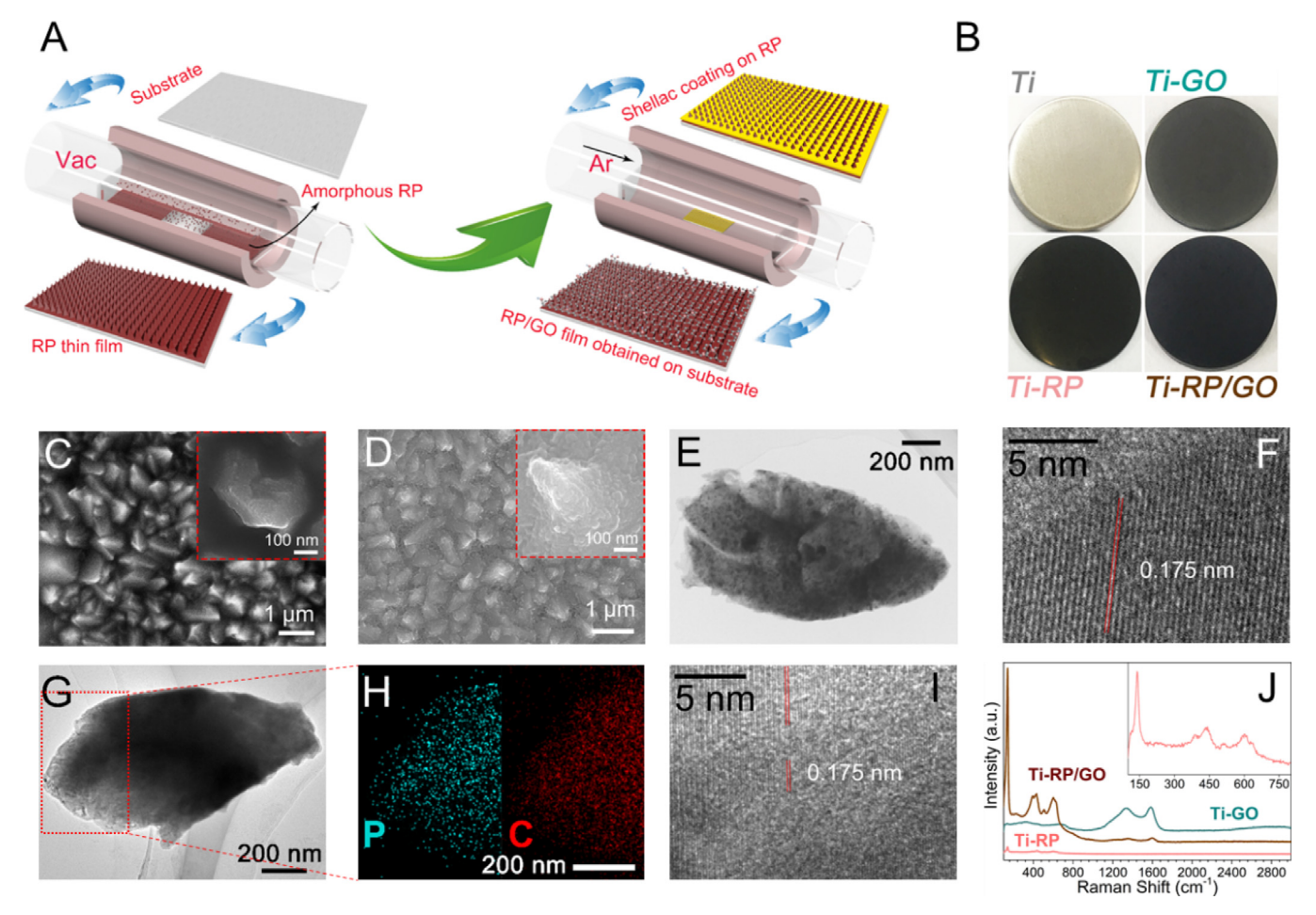


Fig. 1. (A) Schematic diagram of the synthesis process of RP/GO film. (B) Pictures of the samples; SEM images of (C) Ti-RP, (D) Ti-RP/GO. (E) TEM and (F) HRTEM images of Ti-RP. (G) TEM, (H) elemental mapping images of C, P and (I) HRTEM of Ti-RP/GO. (J) Raman spectra of the samples.

RP/GO further support the conclusion (Fig. S3C and D).

Fig. S4A showed that RP powder was amorphous [28]. After the CVD treatment, the crystalline peaks of Ti-RP appeared (Fig. S4B), which suggested that the crystal transition occurred of amorphous RP. Besides, the patterns also suggest the successful preparation of RP/GO.

In the Fig. 1J, the Ti-GO and Ti-RP/GO both showed the G peak, indicating the production of sp² bonded carbon atoms [37]. Also, the observed D and 2D peaks indicated defects in sp² carbon network, which were explored later by XPS. Besides, the differences between Ti-RP and RP powder, in peaks of Raman spectra at 350–650 cm⁻¹ (Fig. S4C), also revealed a significant phase change of RP powder in the CVD treatment. Also, the combined peaks of Ti-RP/GO illustrated the successful transformation of GO layer on RP film.

XPS was used to investigated the chemical bonding between RP and GO layers, as well as the attached oxygen functional groups in the GO. The P 2p spectra of Ti-RP/GO was fitted to three peaks at 132.7 eV (P-C), 133.5 eV (P-P) and 134.7 eV (P-O), respectively (Fig. 2A) [38]. Compared to Ti-RP, a new peak of P-C appeared in Ti-RP/GO. The C 1 s spectra of Ti-GO showed peaks at 284.5 eV (C=C/C-C), 285.4 eV (C-O), 286.3 eV (C=O), and 288.1 eV (O-C=O), respectively (Fig. 2B) [37,38]. Compare to Ti-GO, the new peak at 283.8 eV in Ti-RP/GO was also attributed to the C-P bond. The results proved the formation of chemical bonding between the RP and GO. And the D peak and the weak 2D peak would be attributed by the oxygen functional groups of the GO. In addition, because of the same method and consistent results, the film transformed from shellac was also termed ass graphene oxide according to the previous reports [37,39].

3.2. Photoelectrochemical (PEC) performance test and energy band distribution

The charge transfer properties were investigated by PEC experiments under SSL. When the electrode absorbed light, the photo-generated carriers would be rapidly separated and diffused to the interface of the electrode/electrolyte, which would result in the establishment of a double electric layer and the generation of the open circuit potential (OCP). The OCP parameter reflects the amount of charge transported by photo-generated carriers to the surface of the film. Fig. 2C showed the OCP of Ti-GO was shift from $-134.7\,\text{mV}$ to $-231.1\,\text{mV}$ $(\Delta OCP = 96.4 \, mV)$ after irradiation, while that of Ti-RP/GO was shift from $-34.2 \,\text{mV}$ to $-335.3 \,\text{mV}$ ($\Delta OCP = 301.1 \,\text{mV}$). The enhance demonstrated that the electrons in RP film could transfer into GO layer and then to the interface of the electrode/electrolyte [40]. Throughout the whole potential range, Ti-RP/GO exhibited a higher current density under irradiation (Fig. 2D). As comparison, the current densities without irradiation were relatively negligible. The photocurrent density of Ti-RP/GO under the bias of 0.8 V vs. Ag/AgCl was about 1.2 mA·cm⁻², which was about four-fold than Ti-GO (about 0.3 mA·cm⁻²) and three-fold than Ti-RP (about 0.4 mA·cm⁻²). The results revealed that more charge carriers were produced from the composite. The consistent conclusion was also supported by Fig. 2E, which would be attributed by the efficient electron transfer from RP to GO layer with the higher separation efficiency.

Due to effective transfer of the carriers, the photocarrier transfer barrier of RP/GO was declined apparently (Fig. 2F). Clearly, the smaller semicircle at intermediate frequency revealed that Ti-RP/GO had a

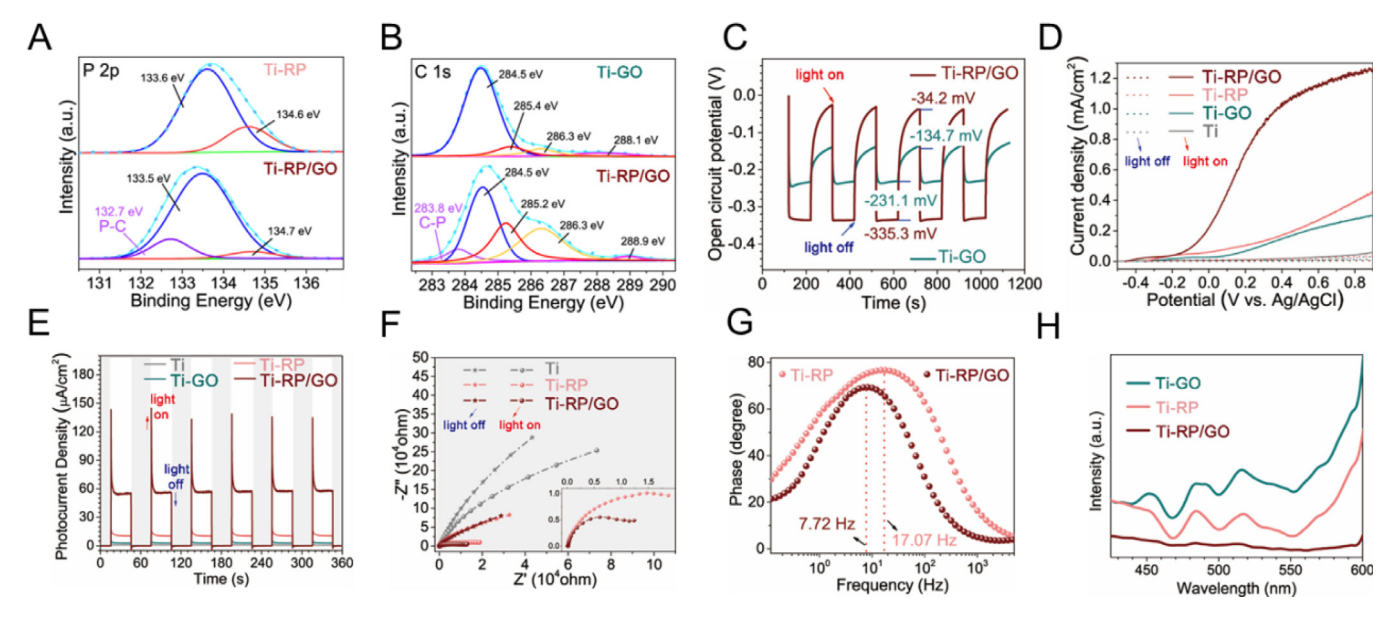


Fig. 2. High-resolution XPS spectra for (A) P 2p of Ti-RP and Ti-RP/GO, (B) C1s of Ti-GO and Ti-RP/GO. Photoelectrochemical (PEC) measurements, including (C) open circuit potential (OCP) response, (D) Linear sweep voltammetry (LSV) scanning, (E) photocurrent responses, (F) electrochemical impedance spectra (EIS), and (G) bode phase plots. (H) Photoluminescence spectra of samples.

decreased interface resistance and consequently facilitated charge transport and transfer [41]. Furthermore, the corresponding Bode phase plots were used to calculated the lifetime of photogenerated electron (τ_n) according to the following equation (Fig. 2G).

$$\tau_n = 1/(2\pi f_{max})$$

where f_{max} is the maximum frequency corresponding to the phase angle peak in the intermediate frequency region [40].

The calculated electron life times were 9.3 ms for Ti-RP and 20.6 ms for Ti-RP/GO. The enhancement indicated the lower recombination rate in Ti-RP/GO. It is worth noting that the carriers transfer kinetics of RP film could be indeed facilitated through hybrid. The high carriers mobility of GO facilitated the charge separation process in RP/GO. In addition, the photoluminescence (PL) spectra confirms the interpretation (Fig. 2H). The PL spectra showed the quenched characteristic peak (from 470 nm to 550 nm) of Ti-RP/GO, suggesting the longer lifetime of electrons and the slower recombination process. Based on above, Ti-RP/GO was expected to exhibit improved photocatalytic activity.

To investigate the band structure, UV–Vis diffuse reflectance spectra (DRS), Mott-Schottky (MS) plots and XPS valence spectra were utilized. The Tauc plots from DRS were used to obtain the bandgaps (E $_g$) (Fig. 3A) [42,43]. The E $_g$ of RP was 0.85 eV and that of GO was ranged from 1.09 to 3.50 eV (Fig. S5) [44,45]. The MS plots were employed to further investigate the conduction band (CB) (Fig. 3B) [46]. The electrochemical flat-band potential (E $_{fb}$) were $-0.94\,V$ and $-0.88\,V$ vs. Ag/AgCl for RP and for GO, respectively. Based on above results, the band structure can be calculated (Fig. 3C). The top of the valence band (VB) were also estimated by XPS valence spectra, which showed that the VB of GO is more positive than that of RP (Fig. S6A). It was of good agreement with the calculation.

At last, the energy-band configuration and hypothetical carriers transfer mechanism was drawn in Fig. 3C. The anti-bonding π^* orbital mainly forms the CB edge of GO, while the O 2p orbital mainly forms the VB edge [45]. The localization of the electron-hole pairs on the basal plane of GO was led by the isolated sp² clutters with the oxygenated functional groups, that is, C–O–H and C–O–C [47]. Besides, the E $_g$ of GO was depended on the amount of oxygenated sites, which contributed to the various VB [47]. According to the previous analysis, we assumed that the E $_g$ energy of GO was stretched by the oxygenated components on the basal plane, which helped the electrons excited from

VB to CB. When the hybrid aborted light, RP and GO would be excited to generate electro/hole pairs, and then the electrons in the CB of RP transferred to GO. In this way, the adjacent GO acted as the electron acceptor by interfacial P-C bonding at the atomic level, and facilitated the directed charge carrier transport to inhibit charge recombination, thus promoting PEC performance. In addition, the detection of singlet oxygen ($^{1}O_{2}$) by ESR further demonstrated that GO can improve the photocatalytic performance of the RP film (Fig. S6B), which the generation of $^{1}O_{2}$ was closely related to both the electrons and holes [48].

3.3. Photo-driven antibacterial tests

To further understand the photocatalytic ability under SSL and the application prospect, the antibacterial tests of water disinfection were measured. The fluorescent-based cell live/dead assay suggested the bacteria were alive on all samples without irradiation (Fig. 4A). In contrast when with irradiation, partial red fluorescence appeared on Ti-GO and Ti-RP while almost all were red on Ti-RP/GO. This proved the best antibacterial activity of Ti-RP/GO. A few of red fluorescence on Ti would be caused by the ultraviolet portion of the SSL. Besides, based on the spread plate assays, all samples exhibited poor antibacterial activity when without irradiation (Fig. 4B and C). It was consistent with the results of Fig. 4A. When irradiation for 20 min with S. aureus, Ti-RP exhibited an antibacterial efficiency of 78.68%, and showed that of 98.28% after deposition of GO. But when the concentration of bacteria was reduced to 8 × 10⁶ CFU/mL, both Ti-RP and Ti-RP/GO showed antibacterial efficiency of more than 99% (Fig. S7A and Fig. 4D). To prove that Ti-RP/GO was effective against all bacteria and not just gram-positive bacteria, the tests on E. coli were also conducted. After irradiation for 15 min, Ti-RP/GO showed antibacterial effect of 99.91% (Fig. S7B and Fig. 4E). The corresponding fluorescent-based cell live/ dead assay was also agree with the result (Fig. S7C). Moreover, in the recycling test represented by S. aureus, the antibacterial activity could last at least 5 cycles without obvious decay (Fig. 4F and Fig. S8), in particular 1 h of continuous irradiation was applied before the first cycle. Fig. 4G showed the antibacterial experiment process. The antibacterial tests were carried out in a 96-well plate, where there were a substrate with an effective area (S) of 32 mm² and the bacteria inoculum with a volume (V) of 200 μ L and the concentration (C) of about 1.0×10^7 CFU/mL. Based on the above, it could be inferred that at least

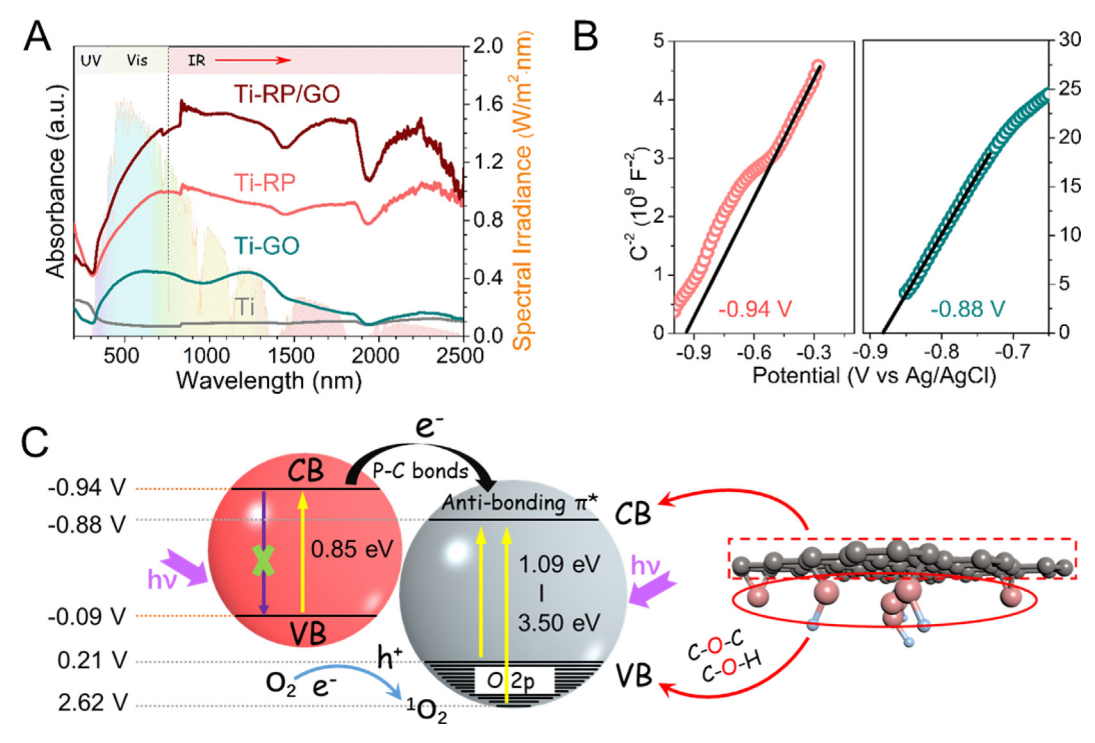


Fig. 3. (A) DRS of the samples. The colorized background is a solar irradiation spectrum. (B) MS plots of Ti-RP and Ti-GO. (C) Schematic of the mechanism to enhance PEC performance.

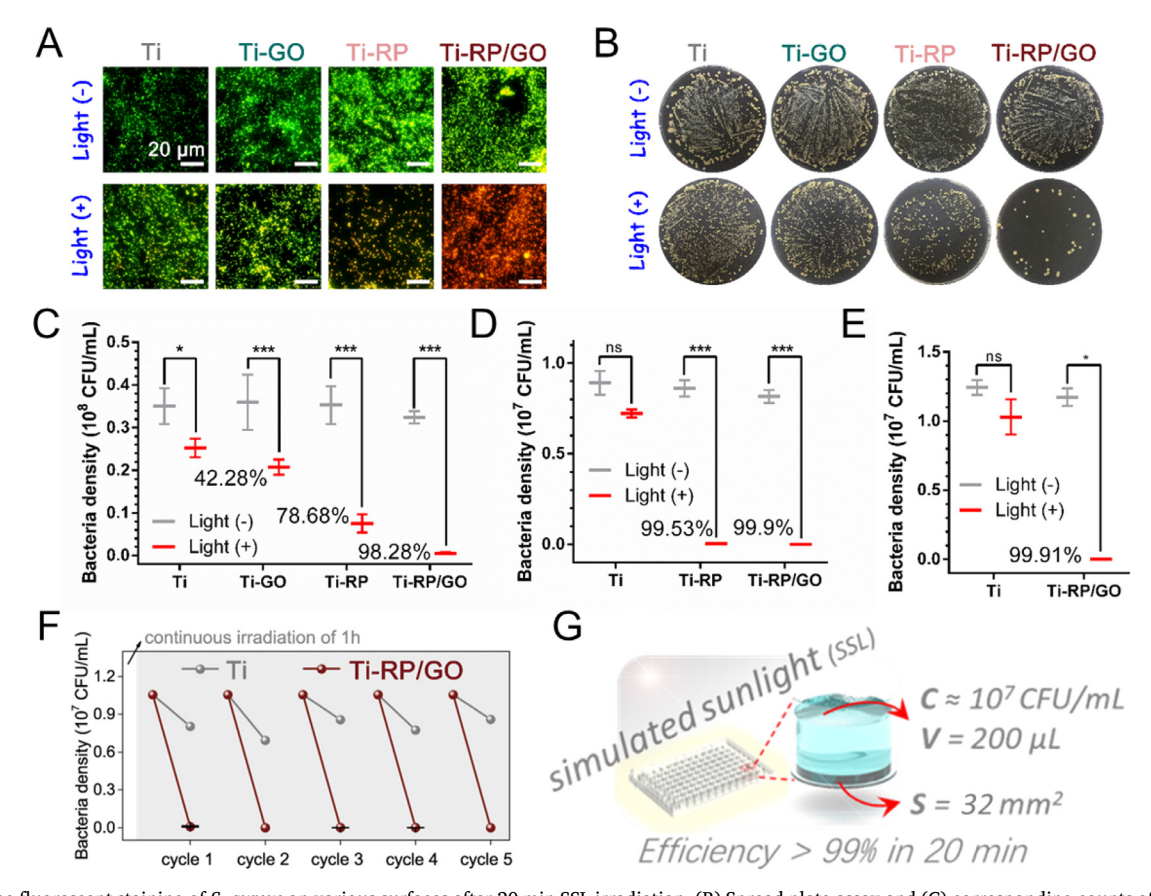


Fig. 4. (A) The fluorescent staining of *S. aureus* on various surfaces after 20 min SSL irradiation. (B) Spread plate assay and (C) corresponding counts of *S. aureus* after irradiation for 20 min of SSL. The assays counts of (D) *S. aureus* with a lower concentration and (E) *E. coli* cultured with the samples after irradiation of SSL for 20 min (*S. aureus*) or 15 min (*E. coli*). (F) The cyclic stability of Ti-RP/GO for photo-driven inactivation with *S. aureus* as an instance. The sample had been continuously irradiated for 1 h before the first cycle. (G) The schematic diagram of antibacterial tests. The optical density of simulated sunlight (SSL) was 0.2 W/cm² in the above tests.

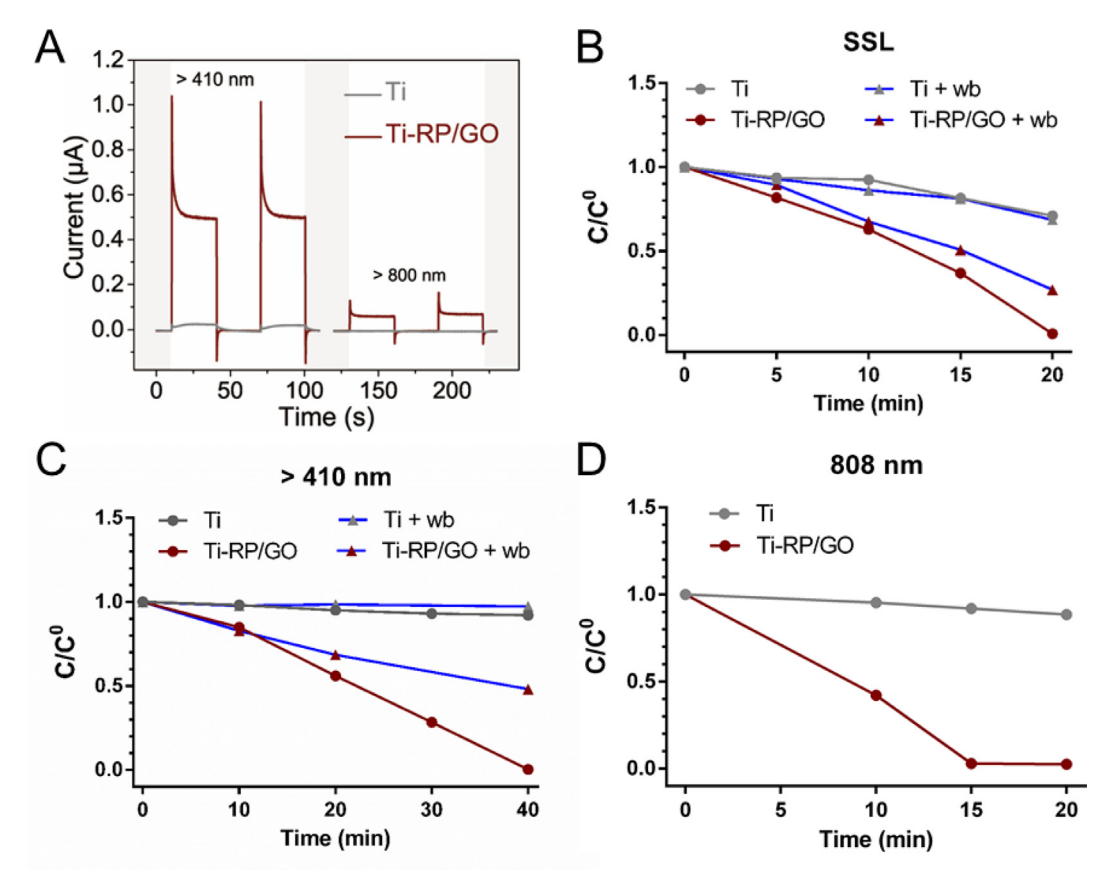


Fig. 5. (A) The photocurrent responses of Ti-RP/GO irradiated by the lights filtered out of SSL by two types of long pass filters. The photo-driven inactivation efficiency of *S. aureus* with the irradiation of (B) SSL (0.2 W/cm^2) , (C) light with wavelength > 410 nm (0.2 W/cm^2) and (D) 808 nm light (0.25 W/cm^2) in infrared region. The 'wb' represented the tests conducted with ice water bath to reduce rise in temperature. The 'C/C⁰' represented the bacterial survival rate.

99% of the bacteria in 200 μL medium were inactivated within 20 min irradiation.

Fig. S9A and B showed the bacterial morphology. As seen, the bacteria on samples without irradiation showed the normal shape. The S. aureus cells showed typical spherical shape with the intact cytoderm, while the E. coli cells showed typical rod-shaped morphology. On the contrary, the cell walls of bacteria (both for S. aureus and E. coli) for all irradiated groups showed varying degrees of damage, such as depression, rupture and deformation (marked with orange or green arrows). It indicated that one of the causes of bacterial death is membrane destruction. Moreover, to further investigate the mechanism of bacterial death, BCA protein leakage analysis (BCA) and adenosine triphosphate measurement (ATP) were conducted (Fig. S9C), using S. aureus as instance. The protein leakage of all the samples except Ti increased significantly under irradiation and the group of Ti-RP/GO increased the most. The result would be due to the highest ROS yield. As the most direct source of energy in bacteria, ATP reflects the metabolism of bacteria. As seen, the level of ATP was lowest in the group of Ti-RP/GO, which was consistent with the best antibacterial efficiency. As comparison, the level of ATP in the groups of Ti-RP was relatively low, together along with the lower photocatalytic performance. The results may be due to the antibacterial mechanism of the synergistic ROS with heat (discuss below), that is, heat inhibits the activity of proteins and the metabolism of bacteria while ROS oxidizes cell membrane and intracellular proteins, interferes with the normal physiologic activities of bacteria, and finally causes the destruction of bacterial membrane and the death of bacteria [49].

Besides, as a schematic diagram shown in Fig. S9D, the germicidal effect does not show any specificity on gram-negative and gram-positive bacteria. Obviously, the antibacterial mechanism by Ti-RP/GO is different from that of antibiotics, which often act on a specific path in

the organism and take a long time to exert effect. Therefore, our strategy would not end up leading to resistance as antibiotics do and causing secondary pollution [2]. The property is essential for water disinfection. Moreover, the photocatalysis was grown on a substrate with an good stability, which makes it extremely easy to reuse and even can be used as a fixed device for the continuous purification of drinking water.

3.4. Photothermal performance

To explore the inherent photothermal properties and support the 'heat' mentioned above, the photothermal performance experiment was conducted. The samples were placed in 200 µL water or in air (Fig. S10), and then irradiated by SSL (0.2 W/cm² or 0.6 W/cm²). Multiple parameters were used to exclude contingency of the trends in photothemal curves. The temperature of Ti-GO was close to Ti at the same time while that of Ti-RP/GO was very close to Ti-RP, and clearly temperature differences existed between the two groups. In this way, GO would only act as photoabsorber to improve the absorbance of the film, thus improving the photothermal property of the RP/GO film. Besides, the crystallization RP would be a potentially ideal solar thermal materials [50], due to its extensive absorption, abundant P reserves and the simple method. Moreover, since the heat difference were little between Ti-RP/GO and Ti-RP, the improvement of the antibacterial performance of Ti-RP/GO would be mainly attributed to the increase of ROS, thus a stronger synergistic effect.

3.5. Antibacterial tests by the irradiation of different wavelengths light.

To explore the performance of Ti-RP/GO under the light of different wavelengths, photocurrent response and antibacterial experiments

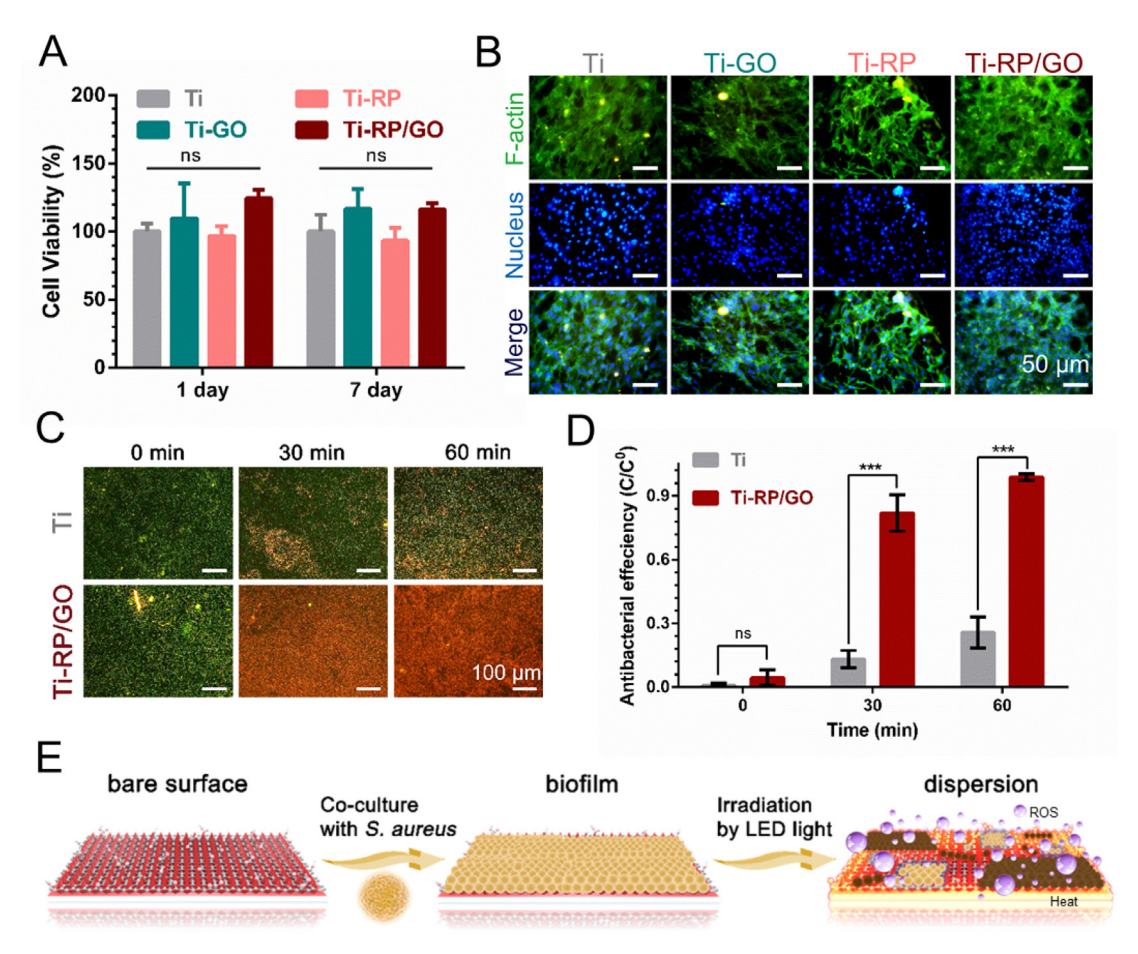


Fig. 6. Cellular response of (A) cytotoxicity of the samples after co-culturing for 1 day and 7 day with NH3T3 cells and (B) fluorescence staining on the surfaces of the samples after co-culture with NH3T3 cells for 24 h. (C) The fluorescent assay of *S. aureus* biofilm after irradiation of LED light (0.1 W/cm²). Green represents living bacteria while red represents dead ones. (D) Quantitative analysis of the fluorescent assay by software Image J. (E) The schematic diagram of biofilm dispersion.

were conducted. Ti-RP/GO showed the photocurrent response under the light with the wavelength $> 410 \, \text{nm}$ or $> 800 \, \text{nm}$ (Fig. 5A). The above lights were generated by the SSL passing through two types of long pass filters. The photocurrent decreased with the decrease of wavelength range, which could be attributed to the decrease in energy of lights as the wavelength range decreases. Of course, GO, a partially insulating semiconduction like material, also got less photoexcitation and ultimately only existed as an electron acceptor [45]. The situation would also lead to a decrease of photocurrent. Moreover, the actual antibacterial efficiency of Ti-RP/GO under different illumination were explored (Fig. 5B-D). The corresponding spread plate assay and bacterial density counts were also given in Figs. S11-S13, in which the antibacterial tests with water bath were for minimizing the effects of heat. In irradiated groups, Ti-RP/GO ultimately showed excellent antibacterial efficiencies, which revealed that Ti-RP/GO could respond to a broad spectral range in the actual solar water disinfection. The decline of bacterial density in the groups of Ti and Ti + wb irradiated by SSL can be attributed to the bactericidal effect of ultraviolet (Fig. 5B). Besides, the antibacterial effect of Ti-RP/GO decreased after the ultraviolet is filtered out, but can still reach the same degree when the time is increased to 40 min (Fig. 5C). The antibacterial effect under 808 nm light (0.25 W/cm²) was also effective (Fig. 5D). The less antibacterial time would be due to low initial bacterial concentration, and the stronger photothermal effect under 808 nm light, which caused the better synergistic effect with the ROS (Fig. S13C and D). Importantly, the water bath experiments excluded the conclusion that the antibacterial effect was all attributed to the influence of high heat. Furthermore, the antibacterial experiments under only heat also supported the conclusion (Fig. S14).

3.6. Biocompatibility evaluation and biofilm removal

At last, the biocompatibility of the samples was evaluated by the 3-[4, 5-dimethylthiazol-2-yl]-2, 5-diphenyl tetrazolium bromide (MTT) assay and fluorescence staining [49,51]. The samples were co-cultured with cells (NIH3T3) for 1 and 7 day, respectively. No significant differences were found between the groups at 1 day (Fig. 6A). As for longer incubation of 7 day, a same trend was observed. The results revealed a similar biocompatibility of RP and RP/GG film compared with Ti. Fig. 6B showed that well-spread cells filled the surfaces of all samples in the vision, which proved the good biocompatibility. This result is consistent with MTT of 1 day. By the way, Fig. S15A showed that the metal-free films owned good hydrophilicity [52,53], which may contribute to the good biocompatibility [13].

With the well biocompatibility, we also explored the application for disinfection of medical device surfaces by LED light [54]. The fluor-escent-based cell live/dead assay of biofilm and the corresponding quantification was shown in Fig. 6C and D. The antibacterial efficiency was > 70% after 30 min irradiation, and could reached > 90% with another 30 min irradiation. Fig. 6E showed the growth and dispersion process of biofilm on the film. Firstly, the samples were co-cultured with the inoculum of *S. aureus* with the concentration of about 10^{10} CFU/mL for 48 h to acquire biofilm. Then the samples were irradiation by the LED light to destructed the biofilm. Once the surface was attacked by the microbes, the deposited film could exhibit an intrinsic biocidal activity as photothermal property (Fig. S15B) and ROS. By the way, ROS were produced under LED light with the presence of O_2 or H_2O , then lipids, proteins, DNA, and RNA would be rapidly destroyed by ROS, leading to bacterial inactivation [55].

Also, the same method was used for depositing RP films on various materials other than Ti plate (Fig. S16). As seen, a black film can be formed uniformly on the surface of various materials, such as Fe, Ni, glass, and TiO2. It was bound to increase the application prospects of the film.

4. Conclusions

In summary, we constructed an irregular pyramid array of crystalline P on Ti, which was efficient to harvest the SSL for photocatalysis and photothermal performance. In addition, the deposition of GO enhanced the absorbance and assisted electron-hole pair separation to improve the photoelectrical performances. In this way, the metal-free RP/GO film showed rapid inactivation of about 99.9% towards S. aureus and E. coli about 1×10^7 CFU/mL within 20 min irradiation of SSL. Also, good antibacterial effects were under visible (> 410 nm), infrared (808 nm) and LED light. Moreover, good biocompatibility enabled application in medical devices disinfection. Since the simple method, low-cost raw materials and effective microbial inactivation, the metal-free hybrid would have large prospect for the photo-driven disinfection of drinking water and medical devices.

Acknowledgements

This work is jointly supported by the National Natural Science Foundation of China, Nos. 51671081, 51871162, 51801056 and 51422102, and the National Key R&D Program of China No. 2016YFC1100600 (sub-project 2016YFC1100604), and Natural Science Fund of Hubei Province, 2018CFA064.

Appendix A. Supplementary data

Supplementary data to this article can be found online at https:// doi.org/10.1016/j.cej.2019.123088.

References

- [1] B. Allegranzi, S.B. Nejad, C. Combescure, W. Graafmans, H. Attar, L. Donaldson, D. Pittet, Burden of endemic health-care-associated infection in developing countries: systematic review and meta-analysis, Lancet 377 (2011) 228-241.
- [2] A.Y. Peleg, D.C. Hooper, Hospital-acquired infections due to gram-negative bacteria, N. Engl. J. Med. 362 (2010) 1804-1813.
- [3] Q. Li, S. Mahendra, D.Y. Lyon, L. Brunet, M.V. Liga, D. Li, P.J.J. Alvarez, Antimicrobial nanomaterials for water disinfection and microbial control: potential applications and implications, Water Res. 42 (2008) 4591-4602.
- P.J.J. Alvarez, C.K. Chan, M. Elimelech, N.J. Halas, D. Villagrán, Emerging opportunities for nanotechnology to enhance water security, Nat. Nanotechnol, 13 (2018) 634-641.
- [5] S. Ma, S. Zhan, Y. Jia, Q. Shi, Q. Zhou, Enhanced disinfection application of Agmodified g-C₃N₄ composite under visible light, Appl. Catal. B: Environ. 186 (2016)
- B. Jalvo, M. Faraldos, A. Bahamonde, R. Rosal, Antibacterial surfaces prepared by electrospray coating of photocatalytic nanoparticles, Chem. Eng. J. 334 (2018) 1108-1118.
- [7] K.H. Park, G.D. Han, K.C. Neoh, T.S. Kim, J.H. Shim, H.D. Park, Antibacterial activity of the thin ZnO film formed by atomic layer deposition under UV-A light, Chem. Eng. J. 328 (2017) 988-996.
- Y. Zhu, X. Liu, K.W.K. Yeung, P.K. Chu, S. Wu, Biofunctionalization of carbon nanotubes/chitosan hybrids on Ti implants by atom layer deposited ZnO nanostructures, Appl. Surf. Sci. 400 (2017) 14-23.
- Y. Liu, H.C. van der Mei, B. Zhao, Y. Zhai, T. Cheng, Y. Li, Z. Zhang, H.J. Busscher, Y. Ren, L. Shi, Eradication of multidrug-resistant staphylococcal infections by lightactivatable micellar nanocarriers in a murine model, Adv. Funct. Mater. 27 (2017) 1701974
- [10] C.M. Courtney, S.M. Goodman, T.A. Nagy, M. Levy, P. Bhusal, N.E. Madinger, C.S. Detweiler, P. Nagpal, A. Chatterjee, Potentiating antibiotics in drug-resistant clinical isolates via stimuli-activated superoxide generation, Sci. Adv. 3 (2017)
- [11] P. Cheng, Q. Zhou, X. Hu, S. Su, X. Wang, M. Jin, L. Shui, X. Gao, Y. Guan, R. Nözel, G. Zhou, Z. Zhang, J. Liu, Transparent glass with the growth of pyramid-type MoS₂ for highly efficient water disinfection under visible-light irradiation, ACS Appl. Mater. Interfaces 10 (2018) 23444-23450.
- [12] C. Liu, D. Kong, P. Hsu, H. Yuan, H. Lee, Y. Liu, H. Wang, S. Wang, K. Yan, D. Lin, P. Maraccini, K. Parker, A. Boehm, Y. Cui, Rapid water disinfection using vertically

- aligned MoS₂ nanofilms and visible light, Nat. Nanotechnol. 11 (2016) 1098. [13] L. Tan, J. Li, X. Liu, Z. Cui, X. Yang, S. Zhu, Z. Li, X. Yuan, Y. Zheng, K.W.K. Yeung,
- H. Pan, X. Wang, S. Wu, Rapid biofilm eradication on bone implants using red phosphorus and near-infrared light, Adv. Mater. 30 (2018) 1801808.
- J. Li, X. Liu, L. Tan, Y. Liang, Z. Cui, X. Yang, S. Zhu, Z. Li, Y. Zheng, K.W.K. Yeung, X. Wang, S. Wu, Light-activated rapid disinfection by accelerated charge transfer in red phosphorus/ZnO heterointerface, Small Methods 3 (2019) 1900048.
- [15] Z. Hu, Z. Shen, J.C. Yu, Phosphorus containing materials for photocatalytic hydrogen evolution, Green Chem. 19 (2017) 588-613.
- [16] B. Yang, J. Yin, Y. Chen, S. Pan, H. Yao, Y. Gao, J. Shi, 2D-black-phosphorus-reinforced 3D-printed scaffolds: a stepwise countermeasure for osteosarcoma, Adv. Mater, 30 (2018) 1705611.
- X. Yang, D. Wang, Y. Shi, J. Zou, Q. Zhao, Q. Zhang, W. Huang, J. Shao, X. Xie, X. Dong, Black phosphorus nanosheets immobilizing Ce6 for imaging-guided photothermal/photodynamic cancer therapy, ACS Appl. Mater. Interfaces 10 (2018)
- [18] Z. Shen, S. Sun, W. Wang, J. Liu, Z. Liu, J. Yu, A black-red phosphorus heterostructure for efficient visible-light-driven photocatalysis, J. Mater. Chem. A 3
- [19] W. Li, Y. Zhang, G. Tian, S. Xue, Q. Xu, L. Wang, J. Tian, Y. Bu, Fabrication of graphene-modified nano-sized red phosphorus for enhanced photocatalytic performance, J. Mol. Catal. A: Chem. 423 (2016) 356-364.
- [20] F. Wang, W.K.H. Ng, J.C. Yu, H. Zhu, C. Li, L. Zhang, Z. Liu, Q. Li, Red phosphorus: An elemental photocatalyst for hydrogen formation from water, Appl. Catal. B: Environ. 111 (2012) 409-414.
- [21] L. Jing, R. Zhu, D.L. Phillips, J.C. Yu, Effective prevention of charge trapping in graphitic carbon nitride with nanosized red phosphorus modification for superior photo(electro)catalysis, Adv. Funct. Mater. 27 (2017) 1703484.
- J. Wang, D. Zhang, J. Deng, S. Chen, Fabrication of phosphorus nanostructures/ TiO₂ composite photocatalyst with enhancing photodegradation and hydrogen production from water under visible light, J. Colloid Inter. Sci. 516 (2018) 215-223
- [23] Y. Zhu, J. Li, C. Dong, J. Ren, Y. Huang, D. Zhao, R. Cai, D. Wei, X. Yang, C. Lv, W. Theis, Y. Bu, W. Han, S. Shen, D. Yang, Red phosphorus decorated and doped TiO₂ nanofibers for efficient photocatalytic hydrogen evolution from pure water, Appl. Catal. B: Environ. 255 (2019) 117764.
- [24] E. Liu, L. Oi, J. Chen, J. Fan, X. Hu, In situ fabrication of a 2D Ni₂P/red phosphorus heterojunction for efficient photocatalytic H2 evolution, Mater, Res. Bull, 115 (2019) 27-36.
- [25] Y. Yuan, S. Cao, Y. Liao, L. Yin, C. Xue, Red phosphor/g-C₃N₄ heterojunction with enhanced photocatalytic activities for solar fuels production, Appl. Catal. B: Environ, 140 (2013) 164-168.
- [26] W. Wang, G. Li, T. An, D. Chan, J. Yu, P. Wong, Photocatalytic hydrogen evolution and bacterial inactivation utilizing sonochemical-synthesized g-C₃N₄/red phosphorus hybrid nanosheets as a wide-spectral-responsive photocatalyst; the role of type I band alignment, Appl. Catal. B: Environ. 238 (2018) 126–135.
- [27] D. Xia, Z. Shen, G. Huang, W. Wang, J. Yu, P. Wong, Red phosphorus: an earthabundant elemental photocatalyst for "green" bacterial inactivation under visible light, Environ. Sci. Technol. 49 (2015) 6264-6273.
- [28] X. Bai, Y. Du, X. Hu, Y. He, C. He, E. Liu, J. Fan, Synergy removal of Cr (VI) and organic pollutants over RP-MoS₂/rGO photocatalyst, Appl. Catal. B: Environ. 239 (2018) 204-213.
- [29] X. Bai, J. Wan, J. Jia, X. Hu, Y. He, C. He, E. Liu, J. Fan, Simultaneous photocatalytic removal of Cr (VI) and RhB over 2D MoS₂/Red phosphorus heterostructure under visible light irradiation, Mater. Lett. 222 (2018) 187-191.
- [30] H. Dang, X. Dong, Y. Dong, H. Fan, Y. Qu, Enhancing the photocatalytic H₂ evolution activity of red phosphorous by using noble-metal-free Ni(OH)2 under photoexcitation up to 700 nm, RSC Adv. 4 (2014) 44823-44826.
- [31] F. Wang, C. Li, Y. Li, J. Yu, Hierarchical P/YPO4 microsphere for photocatalytic hydrogen production from water under visible light irradiation, Appl. Catal. B: Environ. 119 (2012) 267-272.
- [32] Z. Shi, X. Dong, H. Dang, Facile fabrication of novel red phosphorus-CdS composite photocatalysts for H2 evolution under visible light irradiation, Int. J. Hydrogen Energy 41 (2016) 5908-5915.
- [33] S. Ansari, M. Cho, Highly visible light responsive, narrow band gap ${\rm TiO_2}$ nanoparticles modified by elemental red phosphorus for photocatalysis and photoelectrochemical applications, Sci. Rep. 6 (2016) 25405.
- [34] W. Li, J. Yue, F. Hua, C. Feng, Y. Bu, Z. Chen, Enhanced visible light photocatalytic property of red phosphorus via surface roughening, Mater. Res. Bull. 70 (2015) 13-19.
- [35] L. Qi, K. Dong, T. Zeng, J. Liu, J. Fan, X. Hu, W. Jia, E. Liu, Three-dimensional red phosphorus: a promising photocatalyst with excellent adsorption and reduction performance, Catal. Today 314 (2018) 42-51.
- Z. Hu, L. Yuan, Z. Liu, Z. Shen, J. Yu, An elemental phosphorus photocatalyst with a record high hydrogen evolution efficiency, Angew. Chem. Int. Ed. 55 (2016) 9580-9585
- [37] Y.N. Singhbabu, S.K. Choudhary, N. Shukla, S. Das, R.K. Sahu, Observation of large positive magneto-resistance in bubble decorated graphene oxide films derived from shellac biopolymer: a new carbon source and facile method for morphology-controlled properties, Nanoscale 7 (2015) 6510-6519.
- Y. Liu, A. Zhang, C. Shen, Q. Liu, X. Cao, Y. Ma, L. Chen, C. Lau, T.C. Chen, F. Wei, C. Zhou, Red phosphorus nanodots on reduced graphene oxide as a flexible and ultra-fast anode for sodium-ion batteries, ACS Nano 11 (2017) 5530-5537.
- [39] S. Panda, T.K. Rout, A.D. Prusty, P.M. Ajayan, S. Nayak, Electron transfer directed antibacterial properties of graphene oxide on metals, Adv. Mater. 30 (2018) 1702149.

- [40] Y.Y. Han, X.L. Lu, S.F. Tang, X.P. Yin, Z.W. Wei, T.B. Lu, Metal-free 2D/2D heterojunction of graphitic carbon nitride/graphdiyne for improving the hole mobility of graphitic carbon nitride, Adv. Energy Mater. 8 (2018) 1702992.
- [41] W. Zhang, Y. Li, S. Peng, Facile synthesis of graphene sponge from graphene oxide for efficient dye-sensitized H₂ evolution, ACS Appl. Mater. Interfaces 8 (2016) 15187–15195.
- [42] Y. Li, Y. Hou, Q. Fu, S. Peng, Y. Hu, Oriented growth of ZnIn₂S₄/In(OH)₃ heterojunction by a facile hydrothermal transformation for efficient photocatalytic H₂ production, Appl. Catal. B: Environ. 206 (2017) 726–733.
- [43] W. Zhang, W. Li, Y. Li, S. Peng, Z. Xu, One-step synthesis of nickel oxide/nickel carbide/graphene composite for efficient dye-sensitized photocatalytic H₂ evolution, Catal. Today 335 (2019) 326–332.
- [44] H.C. Shown, Y.C. Hsu, C.H. Chang, P.K. Lin, A. Roy, C.H. Ganguly, J.K. Wang, C.I.Wu. Chang, L.C. Chen, K.H. Chen, Highly efficient visible light photocatalytic reduction of CO₂ to hydrocarbon fuels by Cu-nanoparticle decorated graphene oxide, Nano Lett. 14 (2014) 6097–6103.
- [45] T.F. Yeh, J.M. Syu, C. Cheng, T.H. Chang, H. Teng, Graphite oxide as a photocatalyst for hydrogen production from water, Adv. Funct. Mater. 20 (2010) 2255–2262
- [46] Y. Li, P. Han, Y. Hou, S. Peng, X. Kuang, Oriented Zn_mIn₂S_{m+3}@In₂S₃ heterojunction with hierarchical structure for efficient photocatalytic hydrogen evolution, Appl. Catal. B: Environ. 244 (2019) 604–611.
- [47] H.C. Hsu, I. Shown, H.Y. Wei, Y.C. Chang, H.Y. Du, Y.G. Lin, C.A. Tseng, C.H. Wang, L.C. Chen, Y.C. Lin, K.H. Chen, Graphene oxide as a promising photocatalyst for

- CO2 to methanol conversion, Nanoscale 5 (2013) 262-268.
- [48] Y. Nosaka, A.Y. Nosaka, Generation and detection of reactive oxygen species in photocatalysis, Chem. Rev. 117 (2017) 11302–11336.
- [49] Y. Li, X. Liu, L. Tan, Z. Cui, X. Yang, Y. Zheng, K.W.K. Yeung, P.K. Chu, S. Wu, Rapid sterilization and accelerated wound healing using Zn²⁺ and graphene oxide modified g-C₃N₄ under dual light irradiation, Adv. Funct. Mater. 28 (2018) 1800299.
- [50] Y. Wang, L. Li, N. Deng, Y. Wei, S. Weng, D. Dong, J. Qi, X. Qiu, T. Chen, Wu, High-performance photothermal conversion of narrow-bandgap Ti₂O₃ nanoparticles, Adv. Mater. 29 (2017) 1603730.
- [51] H. Wu, L. Tan, M. Yang, C. Liu, R. Zhuo, Protein-resistance performance of amphiphilic copolymer brushes consisting of fluorinated polymers and polyacrylamide grafted from silicon surfaces, RSC Adv. 5 (2015) 12329–12337.
- [52] H. Wu, X. Zhang, L. Huang, L. Ma, C. Liu, Diblock polymer brush (PHEAA-b-PFMA): microphase separation behavior and anti-protein adsorption performance, Langmuir 34 (2018) 11101–11109.
- [53] M. Yang, L. Tan, H. Wu, C. Liu, R. Zhuo, Dual-stimuli-responsive polymer-coated mesoporous silica nanoparticles used for controlled drug delivery, J. Appl. Polym. Sci. 132 (2015) 42395.
- [54] S. Hogan, N.T. Stevens, H. Humphreys, J.P.O. Gara, E.O. Neill, Current and future approaches to the prevention and treatment of staphylococcal medical device-related infections, Curr. Pharm. Des. 21 (2015) 100–113.
- [55] Y. Si, Z. Zhang, W. Wu, Q. Fu, K. Huang, N. Nitin, B. Ding, G. Sun, Daylight-driven rechargeable antibacterial and antiviral nanofibrous membranes for bioprotective applications, Sci. Adv. 4 (2018) eaar5931.